ChemComm

COMMUNICATION

View Article Online
View Journal | View Issue

Cite this: *Chem. Commun.*, 2026, **62**, 6151

Received 17th January 2026,
Accepted 20th February 2026

DOI: 10.1039/d6cc00340k

rsc.li/chemcomm

Influence of cations on nitrate-to-ammonia synthesis over NiO:SnO_2: insights from differential electrochemical mass spectrometry

Eleazar Castañeda-Morales,†[a] Miguel A. Rodríguez-Olguín,†[b] Fabio A. Gómez-Gómez,[a] Francisco Ruiz-Zepeda,[cd] Han Gardeniers,[b] Arturo Manzo-Robledo*[a] and Arturo Susarrey-Arce*[b]

The electrochemical conversion of nitrate to ammonia is crucial for nitrogen upcycling. This study investigates the effect of electrolyte cations (K^+, Na^+, and Li^+) on nitrate electroreduction using NiO:SnO_2 nanofibers. Among other products, *in situ* differential electrochemical mass spectrometry (DEMS) confirms that NH_3 formation strongly depends on cation identity, inducing a shift in product selectivity from NH_3 to H_2. These results highlight the importance of cation-mediated pathways in aqueous systems and provide insight into ammonia synthesis.

The electrochemical reduction of nitrate (NO_3^-), known as ERN, represents a significant technological response to environmental challenges associated with NO_3^- pollution in water sources. The efficacy of this process largely depends on optimizing the electrolyte environment, which can be fine-tuned through various strategies. One approach is electrolyte engineering, which involves modulating the composition and characteristics of the aqueous solution to increase the formation of reaction products during ERN.[1]

A key focus of electrolyte engineering for ERN has been on the role of alkali metal cations, including Li^+, Na^+, K^+, and Cs^+.[2,3] Variations in their ionic sizes significantly influence the electrochemical behavior at the electrode surface, which, in turn, affects the ERN product distribution.[3] Research indicates that different cations induce distinct changes in the electric double layer that surrounds the electrode, thereby impacting the local pH and stabilization of reaction intermediates.[2–4] This indicates the existence of an interplay between cation size and surface charge density, which can affect the interaction with water molecules localized near the electrode. The charge effect is relevant for proton-coupled electron transfer steps.[5,6] Such proton-coupled electron transfer steps can lead to significant shifts in products from NO_3^- to NH_3, N_2O and NO, among others.

The work by Fajardo *et al.* illustrates variations in product distribution, emphasizing how tailored electrolyte compositions can yield substantial benefits for NH_3 synthesis.[2] For ERN, the authors reported some challenges due to the contemporaneous presence of oxygen, which can complicate the ERN process, as the oxygen reduction reaction (ORR) shares the cathodic space and may interfere with NO_3^- reduction.[2] Aside from the ORR, one can expect the existence of other competing reactions, such as the hydrogen evolution reaction (HER).

Under diverse alkali electrolytes, HER production has been linked to a decrease in the electrode work function. In this case, it has been proposed that this situation can arise from the formation of a pronounced surface dipole field upon the adsorption of alkali cations. On electrode surfaces, these cations may interact with surface states, with their impact being strongly dependent on the ionic radii—Li^+ (~76 pm), Na^+ (~99 pm), and K^+ (~138 pm)—which alter the spatial distribution of charges and local electronic states.[5,6] Although the formation of chemical bonds between alkali cations and dangling bonds remains theoretical mainly, both electronic perturbations and geometric factors are thought to modulate the HER kinetics, indirectly governing the formation of nitrogen intermediates.[5] These considerations highlight the pivotal role of electrolyte interfacial properties in influencing reaction selectivity. The latter suggests that careful consideration of the electrolyte environment, in conjunction with cation selection, is crucial for optimizing ERN.

If ERN is achieved to produce NH_3, the electrochemical reduction of NO_3^- can, in turn, be an environmentally attractive

[a] *Instituto Politécnico Nacional, Laboratorio de Electroquímica y Corrosión, Escuela Superior de Ingeniería Química e Industrias Extractivas, Av. Instituto Politécnico Nacional S/N, Unidad Profesional Adolfo López Mateos, CP 07708 CDMX, Mexico. E-mail: amanzor@ipn.mx*
[b] *Department of Chemical Engineering, Mesoscale Chemical Systems, MESA+ Institute, University of Twente, P. O. Box 217, Enschede 7500AE, The Netherlands. E-mail: a.susarreyarce@utwente.nl*
[c] *Department of Materials Chemistry, National Institute of Chemistry, Hajdrihova 19, 1000, Ljubljana, Slovenia*
[d] *Department of Physics and Chemistry of Materials, Institute of Metals and Technology, Lepi pot 11, Ljubljana, Slovenia*
† These authors contributed equally to this work.

alternative for NH_3 synthesis, which traditionally relies on the Haber–Bosch (HB) process—a method associated with high energy consumption.[4,7] This energy demand extends to the molecular level, where the energy penalty of the N_2 bond is attributed to the high dissociation energy of the triple bond in N_2 being 941 kJ mol^{-1}.[7] Instead of N_2, NO_3^- is an interesting alternative for NH_3 production, as the NO bond has a relatively lower dissociation energy (204 kJ mol^{-1}) compared to N_2.[7] This energy is pivotal for the applicability of the electrocatalyst and electrolytes in the current transitioning industry targeting NH_3.

To date, studies have highlighted the potential of various catalysts, including Cu,[4,8] Ni,[4,8] and Sn,[9] as electrocatalysts for the selective chemical transformation of NO_3^- to NH_3. However, little is reported on the effect of electrolyte cations on product distribution during ERN using mixed-oxide electrocatalysts (NiO and SnO_2), investigated by *in situ* DEMS. Therefore, in this work, we synthesized an electrocatalyst using electrospinning. The electrocatalyst contains NiO and SnO_2, hereafter referred to as NiO:SnO_2. The NiO:SnO_2 electrocatalyst, shaped in the form of nanofibers (NF), is morphologically, chemically, and structurally characterized using scanning electron microscopy (SEM), scanning transmission electron microscopy with energy-dispersive X-ray spectroscopy (STEM-EDX), dark-field STEM imaging, and X-ray diffraction (XRD). Electrochemical characteristics of the NiO:SnO_2 NF were studied using cyclic voltammetry (CV) and electrochemical impedance spectroscopy (EIS). The electrocatalyst's functionality is also assessed using DEMS, in which gas-volatile products are analyzed *in situ*. Experimental details used in this work are provided in the SI.

The study begins with the synthesis of NiO : SnO_2 nanofibers (NFs) *via* electrospinning, utilizing a fixed molar ratio of Ni to Sn of 75 : 25. The NiO : SnO_2 NF ratio has been chosen based on our previous optimization for CO_2 electroreduction, where this composition exhibited superior catalytic activity toward the CO_2 reduction reaction.[10] Here, the optimized oxide system is employed to investigate whether the widely reported cation-dependent behavior in Cu-based NO_3^- reduction catalysts also applies to mixed oxides such as NiO:SnO_2.[3,11] SEM images (Fig. 1a and b) show the fiber-like morphology of NiO:SnO_2 NF with an average diameter of 285 ± 44 nm. The dark-field STEM image (Fig. 1c) reveals that the fibers are composed of compacted nanocrystals approximately 8 ± 3 nm in diameter.

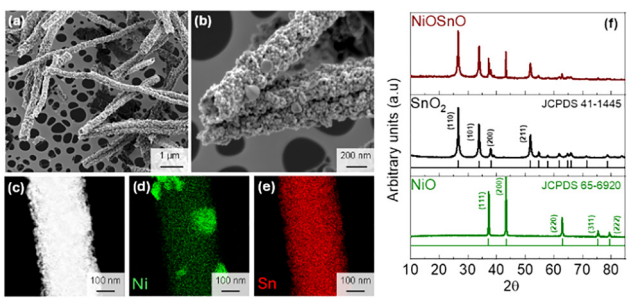

Fig. 1 (a) and (b) SEM images of the produced NiO:SnO_2 NF. The (c) dark-field STEM image and (d) and (e) STEM-EDX maps of NiO:SnO_2 NF. In (f) XRD patterns of NiO, SnO_2, and NiO:SnO_2 NF.

For Ni, the mapping (Fig. 1d) shows Ni to be distributed along the nanofiber body, with the formation of Ni patches, with sizes between 40 and 100 nm. The STEM-EDX mapping of Sn (Fig. 1e) shows a uniform distribution in the NF (Fig. S1).

The NiO:SnO_2 NF structural characterization by XRD is in good agreement with STEM-EDX. XRD demonstrates the formation of NiO and SnO_2. In this case, the diffraction peaks at 2θ = 26.5° (Sn), 33.9° (Sn), 37.2° (Ni), 37.8° (Sn), 43.2° (Ni), and 51.7° (Sn) correspond to NiO and SnO_2 (Fig. 1f).[10] Other crystallographic phases than NiO and SnO_2 have not been found, indicating that NiO and SnO_2 remain in close contact within the nanofiber morphology without necessarily forming other crystallographic phases. The XRD analysis confirms that Ni is predominantly present as Ni^{2+} in the form of crystalline NiO. Higher-valence nickel species (*e.g.*, Ni^{3+}) were also previously identified for the same NiO:SnO_2 NF batch in our earlier work.[10]

In Fig. 2, the *in situ* detection of ERN species is assessed using DEMS. During the electrochemical reduction of NO_3^- from different cations (Li^+, Na^+, and K^+), both faradaic current and ionic current are recorded in a potential window from 0.95 to −0.66 V *vs.* RHE using CV at a scan rate of 1 mV s^{-1} (Fig. 2(a), (f) and (k)). The mass signals detected are ammonia (NH_3, m/z = 17), nitrous oxide (N_2O, m/z = 44), nitric oxide (NO, m/z = 30), and hydrogen (H_2, m/z = 2). Noticeable is the presence of H_2 (Fig. 2(e), (j) and (o)) and NH_3 (Fig. 2(d), (i), and (n)) depending on the cation and the applied potential during steady state conditions at 1 mV s^{-1}, particularly at potentials approximately higher than −0.35 V *vs.* RHE. Interestingly, NO (Fig. 2(c), (h) and (m)) has been found for Li^+ and Na^+. No N_2O fragments are found in Fig. 2 (b), (g) and (l).

The *y*-axis signal corresponding to H_2 (ionic current) varies depending on the nature of the cation. Notably, in the presence of Na^+ cations, a slight inhibition of the HER is observed

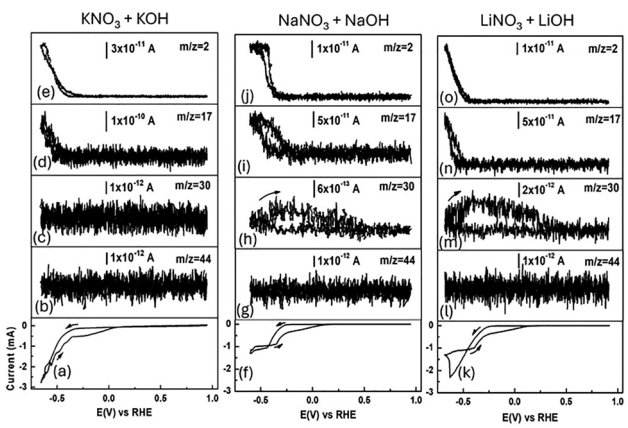

Fig. 2 (a), (f), and (k) Current–potential characteristics of NiO:SnO_2 NFs in the presence of various electrolytes containing: (a) KNO_3 with KOH, (f) $NaNO_3$ with NaOH, and (k) $LiNO_3$ with LiOH. Mass signals as a function of the applied potential for (b), (g) and (l) m/z = 44; (c), (h) and (m) m/z = 30; (d), (i) and (n) m/z = 17; and (e), (j) and (o) m/z = 2. Analyzed mass signals are assigned to H_2 (m/z = 2), NH_3 (m/z = 17), NO (m/z = 30), and N_2O (m/z = 44).

(Fig. 2(j)) when compared to the other two cations. This inhibition becomes more evident when comparing the cell potentials for Li^+, Na^+, and K^+ ions: −0.35 V *vs.* RHE for Na^+, −0.4 V *vs.* RHE for K^+, and −0.45 V *vs.* RHE for Li^+. For the onset of H_2 production, we can then generalize the following trend: $Na^+ < K^+ < Li^+$. These results are crucial because NH_3 production competes with the HER. In this case, the HER can be related to available adsorbed H^+ that react with NO_2^- at the catalyst interface, producing NH_3.

Based on the results from Fig. 2, particularly for Na^+ and Li^+, the rate-determining step could be related to the adsorption of reduced NO_2^- ions from NO_3^-, which influences the generation of NO (eqn (1) and (2)),[12] as can be observed in Fig. 2(c), (h) and (m). To this end, no signal assigned to NO is observed in the presence of K^+ (Fig. 2(c)), indicating faster electron-transfer kinetics toward the formation of NH_3.

$$NO_{2ads}^- + H_2O + e^- \rightarrow NO_{ads} + 2OH^- \quad (1)$$

$$NO_{2ads}^- + 5H_2O + 6e^- \rightarrow NH_{3ads} + 2OH^- \quad (2)$$

The results from the DEMS analysis, as shown in Fig. 2, provide a valuable tool for investigating reaction sequences. For a deeper understanding of the signals shown in Fig. 2, the faradaic current from CVs *vs.* ionic current from the mass signals is shown in Fig. 3(a)–(c). The results facilitate a qualitative comparison during the reduction of NO_3^- to NH_3 (blue line) and the formation of H_2 (black line). Interestingly, competition between H_2 and NH_3 can be observed at moderate overpotentials (from *ca.* −0.2 to −0.45 V *vs.* RHE). In this case, cell potentials higher than −0.45 V *vs.* RHE impose a transport limitation and are therefore not considered.

Additionally, the product distribution for NiO:SnO_2 NF at different supporting electrolytes (K^+, Na^+, Li^+) is shown in Fig. 3(d)–(f). A relatively low H_2 production occurs at low cell potentials, *i.e.*, −0.25 V *vs.* RHE (black bars in Fig. 3(d)–(f)), with Na^+-containing electrolyte, *ca.* <15%. In contrast, at higher cell potentials, it remains close to 32%. However, for other alkali ions, such as K^+ and Li^+, the H_2 product distribution exceeds 32%. In some cases, such as with K^+, the H_2 production reaches up to 95% at −0.45 V *vs.* RHE.

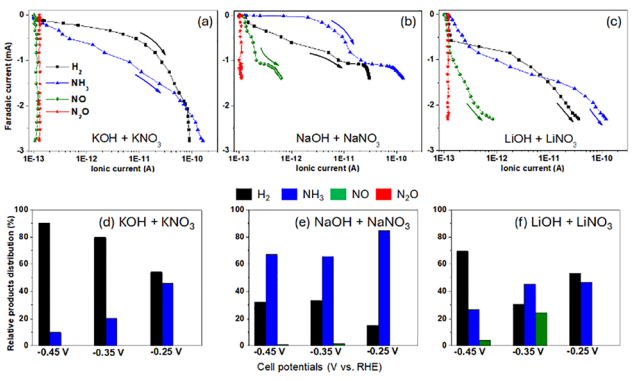

Fig. 3 Faradaic current *vs.* ionic current profiles using DEMS for: (a) KNO_3 with KOH, (b) $NaNO_3$ with NaOH, and (c) $LiNO_3$ with LiOH. (d–f) Relative product distributions estimated from (a)–(c) at different applied potentials (*i.e.*, −0.25, −0.35, and −0.45 V *vs.* RHE).

For NH_3 in Fig. 3(d)–(f), a larger NH_3 production has been observed for the Na^+-containing electrolyte, reaching nearly 90% at −0.25 V *vs.* RHE, and decreasing to approximately 65% at higher cell potentials. This is not the case with other electrolytes, such as K^+ and Li^+, for which a more pronounced variation on the generated product is observed for cell potentials > −0.25 V *vs.* RHE. In this case, K^+ shows a maximum NH_3 product of ~45% at −0.25 V *vs.* RHE, and abruptly decreases at −0.45 V *vs.* RHE (~10%). For Li^+, at −0.35 V, a change in the reaction mechanism may have occurred, with incomplete reduction of NO_3^-, leading to H_2 and NO products, as observed in the CV in Fig. 2(k) at −0.35 V *vs.* RHE. However, this changes at higher cell potentials, yielding H_2 as the major product at −0.45 V *vs.* RHE. Interestingly, oxygenated products, such as NO, have been observed at cell potentials higher than −0.25 *vs.* RHE to be more prominent in Li^+ containing electrolyte. In this case, with −0.35 *vs.* RHE, the NO product is approximately 20%, whereas at −0.45 *vs.* RHE, it is below 5%. Li^+ behavior is attributed to a potential change in the reaction mechanism as indicated by the CV measurements in Fig. 2(k). For Na^+, a NO contribution of around 1.4% or higher has been found, possibly due to the desorption step in eqn (1). For Na^+, a possible explanation is the ORR contribution, which can also lead to oxidized nitrogenated products.[2] However, in our case, it can be excluded. Ar purging was performed for each experiment.

In short, the results of Fig. 3 show that at low cell potentials, the reaction: $NO_3^- + 6H_2O + 8e^- \rightarrow NH_3 + 9OH^-$ is carried out without significant HER competition in the presence of Na^+. In contrast, at higher cell potentials, particularly for K^+ and Li^+, the HER is favored, most probably following the Heyrovsky step: $H_2O + H_{ads} + e^- \rightarrow H_2 + OH^-$.[13] These assumptions are verified from the calculated relationship NH_3/H_2 obtained from Fig. 3(d)–(f), where the ratio is higher for Na^+ with respect to K^+ and Li^+ electrolytes, even as a function of the applied potential, see Table S1. Also, it is essential to note that NO can be produced in the presence of Li^+ and Na^+, indicating a cation-size dependence. The smaller the cation size (*i.e.*, $Li^+ < Na^+ < K^+$), the more NO is produced. The results demonstrate an intimate relationship between alkali cations and NO_3^- ion interaction.[5,6]

EIS is performed to generate insights into the electrochemical processes at the NiO:SnO_2 NFs interface. The corresponding Nyquist plots for NO_3^- in the presence of Li^+, Na^+, and K^+ are presented in Fig. S2. In this case, the diameter of the semicircle in the plots is indicative of the charge transfer resistance, which is influenced by the type of alkali ion used as the supporting electrolyte.[14] The EIS results are associated with an equivalent circuit; the results are shown in Table S2.

Most reported studies on NO_3^- electroreduction have focused on metallic Cu and noble-metal electrodes,[3,11] where alkali metal cations regulate activity and selectivity primarily by modifying the electrical double layer (EDL), the local electric field strength, proton transport, and the stabilization of nitrogen-containing intermediates. In contrast, the present work employs a NiO:SnO_2

oxide heterostructure, whose chemistry is dominated by (non-)oxygenated sites and proton-coupled electron-transfer steps, rendering the reaction pathway particularly sensitive to the interfacial microenvironment rather than solely to intrinsic electron-transfer kinetics.

EIS (Fig. S2 and Table S2) reveals that electrolyte cations (K^+, Na^+, and Li^+) significantly influence the interfacial charge-transfer resistance (R_{ct}) and the accessibility of protons at the electrode surface. While K^+ electrolytes exhibit the lowest R_{ct} ($\approx$ 270 Ω) and higher cathodic currents (-3 mA) in Fig. 2a, indicative of faster interfacial charge-transfer kinetics, this advantage does not translate into an increase in NH_3 production in Fig. 3d. At more negative potentials (≤ -0.45 V), accelerated charge transfer predominantly promotes the HER, yielding H_2 as the dominant product (90%) and concomitantly decreasing the NH_3 fraction to $\sim$10%. The absence of NO products under K^+ conditions further supports a regime dominated by rapid electron transfer rather than controlled NO_3^- hydrogenation. In contrast, Na^+ electrolytes, despite exhibiting higher R_{ct} values than K^+ (Table S2), establish a more favorable interfacial environment for NO_3^- hydrogenation by suppressing the HER and stabilizing hydrogenated nitrogen intermediates.[4–6] This results in a higher NH_3 product (Table S1) across the investigated potential range. Li^+ electrolytes show the highest R_{ct} and intermediate selectivity, further confirming that ammonia formation is governed by cation-dependent reaction branching rather than by charge–transfer resistance alone.

In this work, DEMS provides direct, time-resolved evidence for these trends by resolving the relative formation rates of NH_3, H_2, and NO_x. The DEMS data demonstrate that the identity of the supporting cation dictates product distribution during ERN by modulating the interfacial microenvironment,[3,5,6,11] thereby controlling the competition between NO_3^- hydrogenation and the HER. Overall, these results indicate that, under the current operating conditions, Na^+ is the most favorable electrolyte for selective ammonia synthesis with mixed-oxide NiO:SnO_2 electrocatalysts. Based on our previous results, we propose a reaction sequence, as shown in Fig. S2(b).

In conclusion, a NiO:SnO_2 electrocatalyst has been successfully synthesized using electrospinning. The functionality of the NiO:SnO_2 is assessed during ERN in the presence of three different electrolytes containing Li^+, Na^+, and K^+. DEMS enables the understanding of species generated. H_2, NH_3, and NO have been observed as products. For NH_3 production, a Na^+-containing electrolyte is shown to be the most promising across a range of cell potentials. Na^+ results indicate that moderate electron transfer kinetics (*i.e.*, R_{ct} 335.8) are most suitable for NH_3 production. Our results highlight the intimate relationship between the electrocatalyst and the alkali electrolyte.

E. C-M., M. A. R.-O., F. A. G.-G., and F. R.-Z: writing – original draft, visualization, validation, investigation, formal analysis, and data curation. H. G., A. M.-R., and A. S.-A.: writing – review and editing, supervision, resources, project administration, methodology, funding acquisition, and conceptualization.

Conflicts of interest

There are no conflicts to declare.

Data availability

Data are available upon request from the authors.

The data supporting this article have been included as part of the supplementary information (SI). Supplementary information: STEM-EDX and further experimental details. See DOI: https://doi.org/10.1039/d6cc00340k.

Acknowledgements

M. A. R.-O, A. S.-A., and H. G. are recipients of Horizon 2020 ERC research and innovation programme of the European Union funding under Grant Agreement No. 742004. F. R.-Z. would like to acknowledge the ERC Starting Grant 123STABLE (Grant agreement ID: 852208). This work was financially supported by the SIP-20240528 and 20250900 projects from the Instituto Politécnico Nacional (IPN), Mexico. The authors gratefully acknowledge the CNMN-IPN for providing the characterization facilities. E. C.-M. and F. A. G.-G. acknowledge SECIHTI-Mexico for a Doctorate study fellowship.

References

1 Y. Xiong, Y. Wang, J. Zhou, F. Liu, F. Hao and Z. Fan, *Adv. Mater.*, 2024, **36**, 2304021.
2 A. S. Fajardo, P. Westerhoff, S. García-Segura and C. M. Sánchez-Sánchez, *Sep. Purif. Technol.*, 2023, **321**, 124233.
3 W. Wen, S. Fang, Y. Zhou, Y. Zhao, P. Li and X.-Y. Yu, *Angew. Chem., Int. Ed.*, 2024, **63**, e202408382.
4 E. Castañeda-Morales, J. O. Peralta-Cruz, F. Ruiz-Zepeda, A. Susarrey-Arce, M. L. Hernández-Pichardo and A. Manzo-Robledo, *Mater. Today Energy*, 2024, **41**, 101525.
5 A. Manzo-Robledo, C. Lévy-Clément and N. Alonso-Valente, *Electrochim. Acta*, 2014, **117**, 420–425.
6 M. Muhyuddin, N. Pianta, J. A. Trindell, R. Ruffo, C. Santoro and M. T. M. Koper, *Electrochim. Acta*, 2025, **535**, 146684.
7 F. Han, M. Shi, J. Kim, J. Kim, P. Jeon, J. Noh, K. Im, F. Li, Y. R. Uhm, C. S. Kim, Q. Jiang and B. Baek, *Sci. Adv.*, 2019, **5**, eaax8275.
8 Y. Wang, A. Xu, Z. Wang, L. Huang, J. Li, F. Li, J. Wicks, M. Luo, D.-H. Nam, C.-S. Tan, Y. Ding, J. Wu, Y. Lum, C.-T. Dinh, D. Sinton, G. Zheng and E. H. Sargent, *J. Am. Chem. Soc.*, 2020, **142**, 5702–5708.
9 R. Qi, Q. Jiang, M. Zhong, W. Li, S. Ren, Y. Wang, M. Feng and X. Lu, *J. Chem. Eng.*, 2024, **496**, 154094.
10 M. A. Rodriguez-Olguin, R. Lipin, M. Suominen, F. Ruiz-Zepeda, E. Castañeda-Morales, A. Manzo-Robledo, J. G. E. Gardeniers, C. Flox, T. Kallio, M. Vandichel and A. Susarrey-Arce, *J. Mater. Chem. A*, 2024, **12**, 32821–32835.
11 L.-H. Zhang, Y. Jia, J. Zhan, G. Liu, G. Liu, F. Li and F. Yu, *Angew. Chem., Int. Ed.*, 2023, **62**, e202303483.
12 D. Anastasiadou, Y. van Beek, E. J. M. Hensen and M. Costa Figueiredo, *Electrochem. Sci. Adv.*, 2023, **3**, e2100220.
13 S. González-Poggini, *Int. J. Hydrogen Energy*, 2024, **59**, 30–42.
14 A. R. C. Bredar, A. L. Chown, A. R. Burton and B. H. Farnum, *ACS Appl. Energy Mater.*, 2020, **3**, 66–98.

